Commun. Comput. Phys.
doi: 10.4208/cicp.2014.m343

Vol. **17**, No. 5, pp. 1185-1200
May 2015

Numerical Simulation of Rarefied Gas Flows with Specified Heat Flux Boundary Conditions

Jianping Meng[1,†], Yonghao Zhang[1,*] and Jason M. Reese[2]

[1] *James Weir Fluids Laboratory, Department of Mechanical & Aerospace Engineering, University of Strathclyde, Glasgow G1 1XJ, United Kingdom.*
[2] *School of Engineering, University of Edinburgh, Edinburgh EH9 3JL, United Kingdom.*

Received 30 October 2013; Accepted (in revised version) 10 August 2014

Abstract. We investigate unidirectional rarefied flows confined between two infinite parallel plates with specified heat flux boundary conditions. Both Couette and force-driven Poiseuille flows are considered. The flow behaviors are analyzed numerically by solving the Shakhov model of the Boltzmann equation. We find that a zero-heat-flux wall can significantly influence the flow behavior, including the velocity slip and temperature jump at the wall, especially for high-speed flows. The predicted bimodal-like temperature profile for force-driven flows cannot even be qualitatively captured by the Navier-Stokes-Fourier equations.

AMS subject classifications: 76P05, 82B40

Key words: Thermal boundary condition, rarefied gas flow, S model, discrete velocity method.

1 Introduction

In a broad range of engineering applications involving gas flows the characteristic spatial scale is comparable to the mean free path of the working gas. These applications range from high altitude and high speed space vehicles [1] to Micro-Electro-Mechanical Systems (MEMS) [2]. In such conditions, typically, the conventional Navier-Stokes-Fourier (NSF) equations are inappropriate as rarefaction effects become substantial. Kinetic methods such as direct simulation Monte Carlo (DSMC) [3] and direct solution of the Boltzmann equation [4] become necessary. However, the computational costs of these methods are high. In particular, as the signal/noise ratio is typically low for flows in MEMS the

[†]*Present address:* Scientific Computing Department, STFC Daresbury Laboratory, Warrington WA4 4AD, United Kingdom.
[*]Corresponding author. *Email addresses:* jianping.meng@stfc.ac.uk (J. P. Meng), yonghao.zhang@strath.ac.uk (Y. H. Zhang), jason.reese@ed.ac.uk (J. M. Reese)

computational cost can be prohibitive for DSMC. Various techniques have been proposed to improve computational efficiency, e.g. [5–8].

Thermal management is an aspect of gas flow applications, e.g., re-entry vehicle thermal protection systems in which insulation techniques are used. To describe such systems, it is important to be able to employ constant heat flux boundary conditions so that the heat exchange between the system and the surroundings can be controlled [9–18]. If the surface is well insulated, the adiabatic boundary condition may be appropriate for flow modeling. For this purpose, it is convenient to set the accommodation coefficient in the commonly used Maxwell-type boundary condition to zero, i.e., full specular reflection; see the discussion in [11] and an example in [15]. However, to achieve full specular reflection, the surface should be perfectly smooth at the microscale. For general surfaces, the specified heat flux boundary condition should be achievable even with full diffuse-reflection. A few implementations of this have been explicitly discussed for the DSMC method [9, 10]. However, there is a lack of such discussion for simulations where the kinetic equations themselves are directly solved, even for simple flows.

In this paper, we report our numerical investigations of rarefied gas flows confined between two parallel infinite plates. We solve the Shakhov model (S model) of the Boltzmann equation [19, 20]. While one plate is specified with a constant heat flux (only zero heat flux is simulated in this paper), the other has a fixed temperature. Here we suppose that the zero heat flux boundary closely resembles the adiabatic boundary condition[§]. The numerical method we use is based on the deterministic discrete velocity method (see [21] and references therein). Both a Couette flow and a force-driven Poiseuille flow are examined.

2 Formulation of the problem

2.1 Specification

A monatomic gas is confined between two parallel infinite plates located at $y=0$ and $y=L$. The upper plate ($y=L$) has a fixed temperature, T_0, and the lower one ($y=0$) has a zero heat flux. In Couette flow, the two plates move oppositely with the same speed U_w. For Poiseuille flow, the gas is subject to a uniform external force in the x direction, i.e. the direction parallel to the plates.

2.2 Model

In order to capture rarefaction effects, we solve the S model of the Boltzmann equation, which is given as:

[§]Under rarefied conditions, it becomes rather difficult to precisely define the adiabatic boundary condition, in particular for flows with a moving wall. There may be different kinds of definitions, e.g. [22]. However, we may always use a specified heat flux boundary condition (and not necessarily set to be zero) to describe phenomenologically an "adiabatic" boundary in a practical circumstance.

$$\frac{\partial f}{\partial t}+\boldsymbol{c}\cdot\frac{\partial f}{\partial \boldsymbol{r}}+\boldsymbol{g}\cdot\frac{\partial f}{\partial \boldsymbol{c}}=\frac{1}{\tau}(f_S-f),$$

where $f(\boldsymbol{r},\boldsymbol{c},t)$ is the single molecular velocity distribution function, which describes the number (or portion) of molecules in the volume $d\boldsymbol{r}$ centered at the position $\boldsymbol{r}=(x,y,z)$ with velocities within $d\boldsymbol{c}$ around the velocity $\boldsymbol{c}=(c_x,c_y,c_z)$ at time t. Based on this distribution function, macroscopic quantities such as gas density ρ, velocity $\boldsymbol{u}$, temperature T, stress tensor $\boldsymbol{P}$ and heat flux $\boldsymbol{q}$ can be obtained from its moments i.e.,

$$\rho[1,u_i,3RT,P_{ij},2q_i]=\int[1,c_i,C_iC_i,C_iC_j,C_iC_jC_j]fd\boldsymbol{c},$$

where $\boldsymbol{C}=\boldsymbol{c}-\boldsymbol{u}$ is the peculiar molecular velocity and R is the gas constant. The relaxation time τ has the form of $\tau=p/\mu$ where p is the pressure and μ the viscosity. The body force $\boldsymbol{g}=(g_x,g_y,g_z)$ is assumed to be independent of the molecular velocity. The "equilibrium" function f_S is proposed to be

$$f_S=f_{eq}\left[1+\frac{1-\mathrm{Pr}}{5}\frac{2q_iC_i}{pRT}\left(\frac{C^2}{2RT}-\frac{5}{2}\right)\right], \tag{2.1}$$

where f_{eq} is the Maxwellian distribution

$$f_{eq}=\rho\left(\frac{1}{2\pi RT}\right)^{3/2}\exp\left[-\frac{C^2}{2RT}\right], \tag{2.2}$$

and Pr is the Prandtl number.

It is convenient to introduce the following dimensionless quantities,

$$\hat{x}_k=\frac{x_k}{L},\quad \hat{u}_k=\frac{u_k}{\sqrt{RT_0}},\quad \hat{t}=\frac{\sqrt{RT_0}t}{L},\quad \hat{g}_k=\frac{Lg_k}{RT_0},\quad \hat{c}_k=\frac{c_k}{\sqrt{RT_0}},\quad \hat{T}=\frac{T}{T_0},$$
$$\hat{f}=\frac{f(RT_0)^{3/2}}{\rho_0},\quad \hat{\rho}=\frac{\rho}{\rho_0},\quad \hat{p}=\frac{p}{p_0},\quad \hat{\mu}=\frac{\mu}{\mu_0},\quad \hat{q}_i=\frac{q_i}{p_0\sqrt{RT_0}},\quad \hat{P}_{ij}=\frac{P_{ij}}{p_0}.$$

Here, we use the subscript 0 to denote reference quantities: for the present problems, most of them correspond to quantities at the upper plate, except that the density ρ_0 should be understood as the average density. With these non-dimensional quantities, the governing equation can then be rewritten as

$$\frac{\partial \hat{f}}{\partial \hat{t}}+\hat{c}_k\frac{\partial \hat{f}}{\partial \hat{x}_k}+\hat{g}_k\frac{\partial \hat{f}}{\partial \hat{c}_k}=-\frac{p_0L}{\mu_0\sqrt{RT_0}}\frac{\hat{p}}{\hat{\mu}}(\hat{f}-\hat{f}^{eq})=-\frac{\hat{\rho}\hat{T}^{(1-\omega)}}{\mathcal{K}}(\hat{f}-\hat{f}^S), \tag{2.3}$$

where $\mathcal{K}$ is defined as

$$\mathcal{K}=\frac{\mu_0\sqrt{RT_0}}{p_0L}.$$

The relevant macroscopic quantities become

$$\begin{bmatrix} \hat{\rho} \\ \hat{\rho}\hat{u}_i \\ \hat{P}_{ij} \\ 3\hat{\rho}\hat{T} \\ 2\hat{q}_i \end{bmatrix} = \int \hat{f} \begin{bmatrix} 1 \\ \hat{c}_i \\ \hat{C}_i\hat{C}_j \\ \hat{C}_i\hat{C}_i \\ \hat{C}_i\hat{C}_j\hat{C}_j \end{bmatrix} d\hat{\boldsymbol{c}}. \tag{2.4}$$

The temperature-dependent viscosity can be expressed as $\mu/\mu_0 = (T/T_0)^\omega$, where ω is related to the molecular interaction model, varying from 0.5 for hard-sphere molecular interactions to 1 for Maxwell molecules. The 'hat' symbol will be omitted hereafter for clarity. A rescaled Knudsen number,

$$Kn = \sqrt{\frac{\pi}{2}}\mathcal{K},$$

is used throughout this work.

3 Numerical method

3.1 Equations for marginal distribution functions

As the flows considered here are one-dimensional, we can introduce the following marginal velocity distribution functions, and the corresponding parts for the "equilibrium" distribution, i.e.,

$$\begin{bmatrix} \varphi_a \\ \varphi_b \\ \varphi_c \\ \varphi_d \\ \varphi_e \\ \varphi_f \end{bmatrix} = \int_{-\infty}^{\infty}\int_{-\infty}^{\infty} \begin{bmatrix} 1 \\ c_x \\ c_x^2 \\ c_z^2 \\ c_x^3 \\ c_x c_z^2 \end{bmatrix} f dc_x dc_z, \tag{3.1}$$

$$\begin{bmatrix} \varphi_{as} \\ \varphi_{bs} \\ \varphi_{cs} \\ \varphi_{ds} \\ \varphi_{es} \\ \varphi_{fs} \end{bmatrix} = \int_{-\infty}^{\infty}\int_{-\infty}^{\infty} \begin{bmatrix} 1 \\ c_x \\ c_x^2 \\ c_z^2 \\ c_x^3 \\ c_x c_z^2 \end{bmatrix} f_S dc_x dc_z = \frac{\rho e^{-\frac{c_y^2}{2T}}}{\sqrt{2\pi T}} \times$$

$$\begin{bmatrix} 1-\frac{1}{5\rho T^3}c_y q_y(\mathrm{Pr}-1)(c_y^2-3T) \\ \frac{1}{5\rho T^3}(\mathrm{Pr}-1)(-c_y^3 q_y u_x - c_y^2 q_x T + 3c_y q_y T u_x + q_x T^2) + u_x \\ \frac{1}{5\rho T^3}(\mathrm{Pr}-1)(-c_y^3 q_y (T+u_x^2) - 2c_y^2 q_x T u_x + c_y q_y T\left(T+3u_x^2\right) + 2q_x T^2 u_x) + T + u_x^2 \\ \frac{1}{5\rho T^2}c_y(\mathrm{Pr}-1)q_y(T-c_y^2) + T \\ \frac{-1}{5\rho T^3}(\mathrm{Pr}-1)(c_y^3 q_y u_x(3T+u_x^2) + 3c_y^2 q_x T(T+u_x^2) - 3c_y q_y T u_x(T+u_x^2) + 3q_x T^2(T-u_x^2)) + u_x(3T+u_x^2) \\ T u_x - \frac{1}{5\rho T^2}(\mathrm{Pr}-1)(q_x T(c_y^2+T) + c_y q_y u_x(c_y^2-T)) \end{bmatrix}. \tag{3.2}$$

With these marginal distribution functions, the macroscopic quantities in Eq. (2.4) can be calculated as

$$\begin{bmatrix} \rho \\ \rho u_x \\ 3\rho T \\ P_{xx} \\ P_{xy} \\ P_{yy} \\ P_{zz} \\ 2q_x \\ 2q_y \end{bmatrix} = \int_{-\infty}^{\infty} \begin{bmatrix} \varphi_a \\ \varphi_b \\ \varphi_c + \varphi_d + c_y^2 \varphi_a \\ \varphi_c \\ \varphi_b c_y \\ c_y^2 \varphi_a \\ \varphi_d \\ -3u_x\varphi_c + \varphi_e - u_x c_y^2 \varphi_a + c_y^2 \varphi_b - u_x \varphi_d + \varphi_f \\ c_y(-2u_x\varphi_b + \varphi_c + c_y^2\varphi_a + \varphi_d) \end{bmatrix} dc_y + \begin{bmatrix} 0 \\ 0 \\ -\rho u_x^2 \\ -\rho u_x^2 \\ 0 \\ 0 \\ 0 \\ 2\rho u_x^3 \\ 0 \end{bmatrix}.$$

It should be noted that, for the unidirectional flows considered here, there are some additional relations, i.e. $u_y = u_z = 0$, $P_{xz} = P_{yz}$ and $q_z = 0$ [23]. Now let

$$\phi = \begin{bmatrix} \varphi_a \\ \varphi_b \\ \varphi_c \\ \varphi_d \\ \varphi_e \\ \varphi_f \end{bmatrix}, \quad \phi_e = \begin{bmatrix} \varphi_{as} \\ \varphi_{bs} \\ \varphi_{cs} \\ \varphi_{ds} \\ \varphi_{es} \\ \varphi_{fs} \end{bmatrix}, \quad S = g_x \begin{bmatrix} 0 \\ \varphi_a \\ 2\varphi_b \\ 0 \\ 3\varphi_c \\ \varphi_d \end{bmatrix},$$

then the governing equation for the six distribution functions can be written as

$$\frac{\partial \phi}{\partial t} + c_y \frac{\partial \phi}{\partial y} = \frac{1}{\mathcal{K}} \rho T^{(1-\omega)}(\phi_e - \phi) + S. \tag{3.3}$$

In particular, if the problem is steady, Eq. (3.3) can be further reduced to

$$c_y \frac{\partial \phi}{\partial y} = \frac{1}{\mathcal{K}} \rho T^{(1-\omega)}(\phi_e - \phi) + S. \tag{3.4}$$

In these equations, the corresponding differential force terms have been transformed into the non-differential source term S by utilizing integration by parts, see [24] for details.

3.2 Scheme

The flows are fully-developed, and we use the discrete velocity method to solve Eq. (3.4). We need to discretize in a two-dimensional space, i.e. one dimension in space y, and the other dimension in molecular velocity space c_y. For the molecular velocity space, Simpson's rule is chosen for c_y, and the grid points (say, N_c points) are distributed uniformly. For the physical space, nonuniform grid points are employed with more points located near the boundaries. To construct this kind of grid distribution, we first obtain a distribution of grid points that become highly dense near the mid-point of the channel by using

$$y_i=\alpha\sinh\left[\frac{\sinh^{-1}\left(\frac{1}{2\alpha}\right)(2i-N)}{N}\right]+\frac{1}{2},\quad i=0,\cdots,N, \tag{3.5}$$

where N is the total number of grid points and α is the parameter determining the nonuniformity. The grid system can then instead be made denser near the wall by utilizing symmetry and translation relations.

Regarding the numerical scheme, we employ a second-order upwind scheme except in the near-wall region where a first-order upwind scheme is used. Therefore, the evolution of ϕ can be written as

$$\phi_i=\frac{c_y\left(\eta_i^2\phi_{i-1}-\phi_{i-2}\right)+dy_i\eta_i(\eta_i-1)(w_i\phi_{e,i}+S_i)}{(\eta_i-1)(\eta_i c_y+c_y+dy_i\eta_i w_i)},\quad c_y>0,\quad i=2,\cdots,N \tag{3.6}$$

and

$$\phi_1=\frac{c_y\phi_0+dy_1S_1+dy_1w_1\phi_{e,1}}{c_y+dyw_1},\quad c_y>0, \tag{3.7}$$

where

$$\begin{aligned} &w_i=\frac{\rho_i T_i^{1-\omega}}{\mathcal{K}},\\ &dy_i=y_i-y_{i-1},\quad i=1,\cdots,N, \end{aligned} \tag{3.8}$$

and

$$\eta_i=\frac{dy_i+dy_{i-1}}{dy_i},\quad i=2,\cdots,N.$$

For simplicity, the equations for $c_y<0$ are omitted here, but these can be easily obtained in a manner similar to the above. Our convergence tests show that the whole scheme can achieve second-order accuracy even though a first order scheme is used at the wall point; this can be attributed to the use of a non-uniform grid. The near-wall accuracy is effectively improved by the very small grid size.

3.3 Boundary conditions

In the present simulations, diffuse reflection boundary conditions are employed. The upper plate has a fixed temperature while the lower plate has a specified heat flux. For convenience, the implementation details of both the fixed-temperature and the specified heat flux boundary will be discussed using the lower wall as an example, which can then be straightforwardly applied to the upper plate as required.

Supposing that the macroscopic properties at the wall, such as the density ρ_w, the velocity $\boldsymbol{u}_w$ and the temperature T_w are known, the outgoing distribution function can be written as follows,

$$f(y=0,c_y>0)=\frac{\rho_w}{(2\pi T_w)^{3/2}}\exp\left(-\frac{C_w^2}{2T_w}\right), \tag{3.9}$$

where $\boldsymbol{C}_w$ is the peculiar molecular velocity at the wall, i.e. $\boldsymbol{c}-\boldsymbol{u}_w$. To implement the specific fixed-temperature and specified heat flux boundary conditions, we need to determine the corresponding macroscopic properties according to the related conservation laws. For simplicity, we first write down the incoming mass flux and heat flux as

$$\mathcal{M}_{in}=\int_{c_y<0}\left|c_y f(y=0,c_y<0)\right|d\boldsymbol{c}, \tag{3.10}$$

$$\mathcal{H}_{in}=\frac{1}{2}\int_{c_y<0}\left|c_y C_w^2 f(y=0,c_y<0)\right|d\boldsymbol{c}. \tag{3.11}$$

According to the principle of the diffuse reflection boundary condition, the outgoing mass flux and heat flux can be easily calculated if ρ_w and T_w are known, i.e.,

$$\mathcal{M}_{out}=\int_{c_y>0}\left|c_y\frac{\rho_w}{(2\pi T_w)^{3/2}}\exp\left(-\frac{C_w^2}{2T_w}\right)\right|d\boldsymbol{c}=\frac{\rho_w\sqrt{T_w}}{\sqrt{2\pi}}, \tag{3.12}$$

and

$$\mathcal{H}_{out}=\frac{1}{2}\int_{c_y>0}\left|c_y C_w^2\frac{\rho_w}{(2\pi T_w)^{3/2}}\exp\left(-\frac{C_w^2}{2T_w}\right)\right|d\boldsymbol{c}=2\sqrt{\frac{2}{\pi}}\rho_w T_w^{3/2}. \tag{3.13}$$

If the wall temperature is fixed, we can use the mass conservation law to determine density, i.e. the incoming mass flux is equal to the outgoing mass flux. Through straightforward calculations, the density at the wall is given as

$$\rho_w=\sqrt{\frac{2\pi}{T_w}}\mathcal{M}_{in}. \tag{3.14}$$

For the wall with a specified heat flux, we need to determine both the density and the temperature via mass conservation and the specified heat flux, i.e., we need to solve two equations:

$$\mathcal{M}_{out}-\mathcal{M}_{in}=0, \tag{3.15}$$

and

$$\mathcal{H}_{out}-\mathcal{H}_{in}=q_{yw}, \tag{3.16}$$

where q_{yw} denotes the specified heat flux at the wall. By solving the two equations simultaneously, the density and temperature can be written as

$$\rho_w=\frac{2\sqrt{2\pi}\mathcal{M}_{in}^{3/2}}{\sqrt{\mathcal{H}_{in}+q_{yw}}}, \tag{3.17}$$

and

$$T_w=\frac{\mathcal{H}_{in}+q_{yw}}{4\mathcal{M}_{in}}. \tag{3.18}$$

Specifically, if q_{yw} is set to be zero, the density and the temperature are

$$\rho_w=\frac{2\sqrt{2\pi}\mathcal{M}_{in}^{3/2}}{\sqrt{\mathcal{H}_{in}}}, \tag{3.19}$$

and

$$T_w=\frac{\mathcal{H}_{in}}{4\mathcal{M}_{in}}. \tag{3.20}$$

Here, we focus on the effect of a zero heat flux boundary condition. For the marginal distribution functions, the boundary condition Eq. (3.9) can be transformed to:

$$\begin{bmatrix}\varphi_{aw}\\ \varphi_{bw}\\ \varphi_{cw}\\ \varphi_{dw}\\ \varphi_{ew}\\ \varphi_{fw}\end{bmatrix}=\int_{-\infty}^{\infty}\int_{-\infty}^{\infty}\begin{bmatrix}1\\ c_x\\ c_x^2\\ c_z^2\\ c_x^3\\ c_xc_z^2\end{bmatrix}f_{eq,w}dc_xdc_z=\frac{\rho_w\exp(-\frac{c_y^2}{2T_w})}{\sqrt{2\pi T_w}}\begin{bmatrix}1\\ u_w\\ T_w+u_w^2\\ T_w\\ (3T_w+u_w^2)u_w\\ T_wu_w\end{bmatrix}.$$

4 Numerical results

In the discrete velocity method, it is important to choose appropriate molecular velocities and spatial grids to ensure simulation accuracy. We perform grid independence tests in both physical and velocity spaces, following the procedure detailed in [24] where two types of errors are evaluated simultaneously to assess simulation accuracy. Both types of error are evaluated at the points $[0,0.1,0.2,\cdots,1]$ including the boundary points. If both types of error for the temperature and velocity in the coarser system are less than 1% compared to the finer system, the coarser system is regarded as sufficient. According to these criteria, we determine appropriately discretized systems (i.e. N and N_c for *each* simulated case), which are listed in Table 1. In terms of the truncation of molecular velocity space, we choose the range $[-20,20]$, which produces nearly identical results for force-driven flow at $Kn=0.05$ and $g_x=1$ as using a wider range of $[-30,30]$.

Table 1: Discretization systems N, N_c for the simulated cases.

Kn	g_x or U_w	N	N_c
$0.05\cdots10$	$U_w=0.2$	200	10000
$0.05\cdots0.6$ and $0.8\cdots10$	$U_w=1.5$	200	10000
0.7	$U_w=1.5$	400	10000
$0.05\cdots3$	$g_x=0.1$ and 1	200	10000
5	$g_x=1$	200	10000
10	$g_x=1$	200	20000
5	$g_x=0.1$	200	20000
10	$g_x=0.1$	200	80000

Typical results for Couette flows are presented in Figs. 1-3. In Figs. 1 and 2 it is found that the viscous heating effect can induce a larger temperature rise at the lower wall. For both $U_w=0.2$ and $U_w=1.5$, the temperature at the upper wall increases with the Knudsen number. However, at the lower wall, it first increases then decreases. For the velocity, the trends are the same for both walls.

In Fig. 3, it is seen that the effect of the zero heat flux boundary on the velocity profile is significant for the high-speed case: we observe significantly different velocity slips at the lower and upper plates. Specifically, the velocity slip at the lower (zero-heat-flux) plate is larger. Interestingly, for the low-speed case, the effect on velocity slip is small. At the upper plate, we observe that the temperature jump effect is relatively stronger for the lower speed case, in comparison to the higher speed case.

Regarding the heat flux, it is of interest to observe that there can be non-zero span-wise heat flux q_y at the lower wall for the larger Knudsen numbers, although a zero heat flux is prescribed. This is certainly due to a non-continuum effect and may be understood as a kind of "heat flux jump". For the stream-wise component, we observe non-zero values that cannot be captured by the NSF equations.

The stresses P_{xx} and P_{xy} show similar behaviors in both cases. Again, the trace-free part of stress $P_{xx}-T$ may not be zero, which cannot be captured by the NSF equations.

The results for force-driven Poiseuille flows are shown in Figs. 4-8. Similar to the Couette flow cases, the zero heat flux boundary induces significantly different velocity slips at the lower and upper plates for the case of $g_x=1$. The velocity slip at the lower wall becomes smaller as the external force increases. There is nearly no difference in velocity slip at the two walls for the small force cases and the temperature jump effect is relatively stronger than the large force case.

It is interesting to note that, similar to the case of two fixed-temperature plates, the temperature profiles are qualitatively different from the NSF prediction over a range of Knudsen numbers. For instance, as shown in Fig. 5, we can see a bimodal-like cross-channel temperature distribution, although the two peaks are unsymmetrical here. This

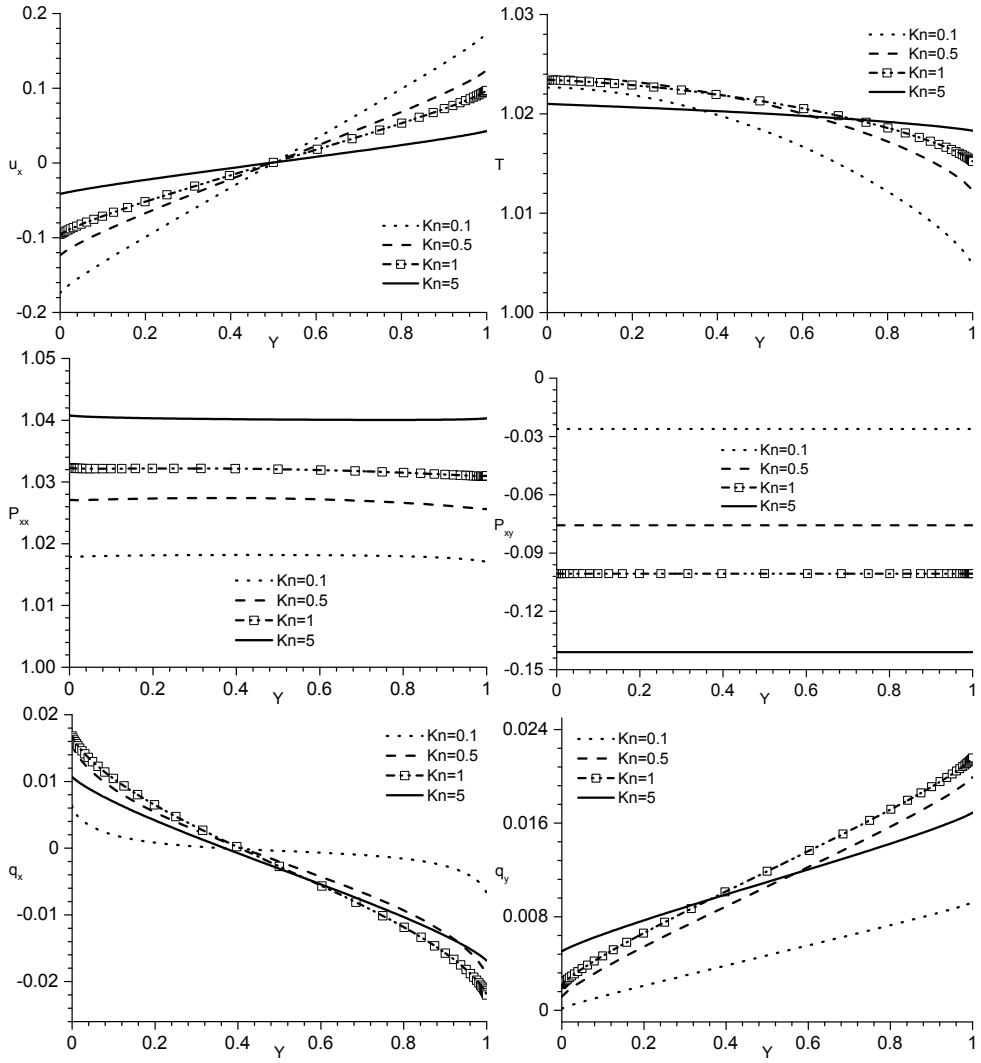

Figure 1: Profiles of macroscopic flow quantities in Couette flows with $U_w = 0.2$. Zero-heat-flux boundary at $Y = 0$, fixed-temperature boundary at $Y = 1$.

is qualitatively different from the NSF prediction in the same figure. The temperature near the zero heat flux wall is often the highest one.

As in the Couette flow, a heat flux jump is observed at the lower wall. There is also a non-zero stream-wise heat flux component, and a non-zero trace-free stress $P_{xx} - T$.

In Fig. 8, we can see that, similar to cases with fixed temperature conditions at the two walls, the Knudsen minimum in the mass flow rate occurs around $Kn = 1$. Since the viscous heating consumes more input work in the larger-force case, the mass flow rates are generally larger for the smaller-force case.

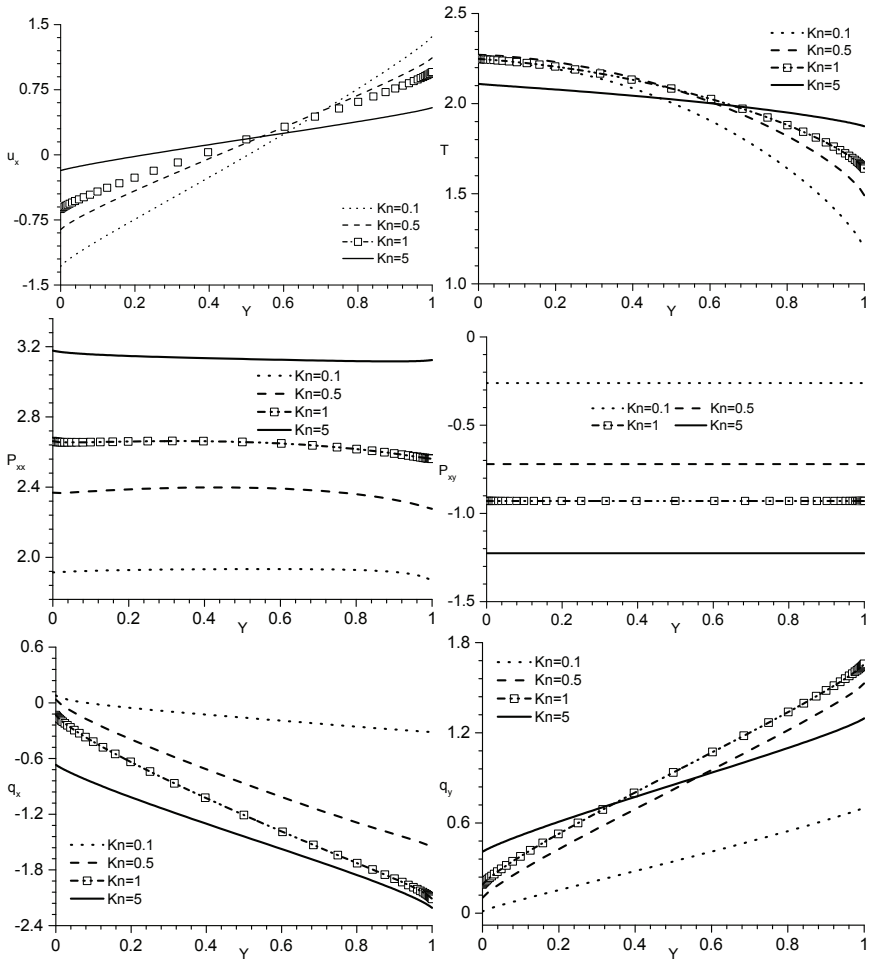

Figure 2: Profiles of macroscopic flow quantities in Couette flows with $U_w = 1.5$. Zero-heat-flux boundary at $Y = 0$, fixed-temperature boundary at $Y = 1$.

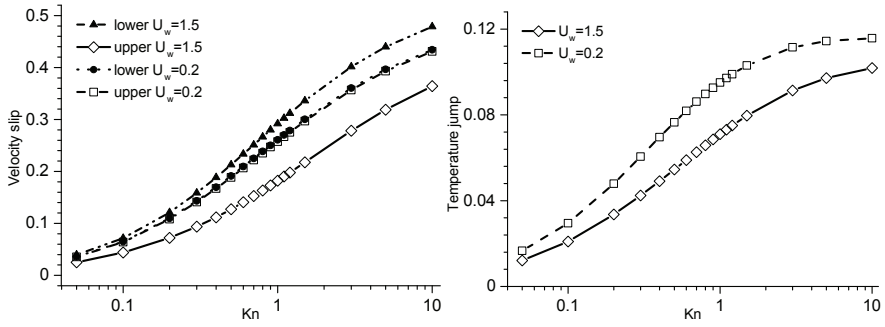

Figure 3: Couette flow; Velocity slip (left) at the lower (zero-heat-flux) and upper (fixed-temperature) plates and (right) temperature jump at the upper plate. The velocity slip is re-normalized by the velocity difference of the two moving plates, and the temperature jump is re-normalized by the square of the velocity difference.

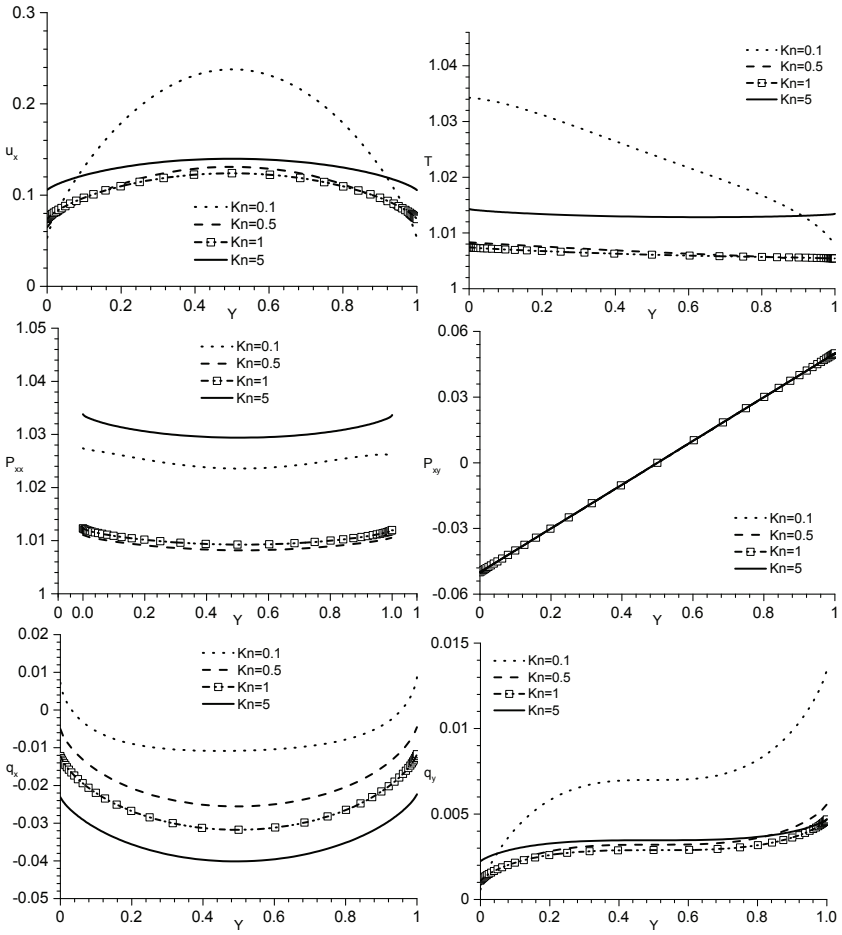

Figure 4: Profiles of macroscopic flow quantities in force-driven Poiseuille flows with $g_x = 0.1$. Zero-heat-flux boundary at $Y = 0$, fixed-temperature boundary at $Y = 1$.

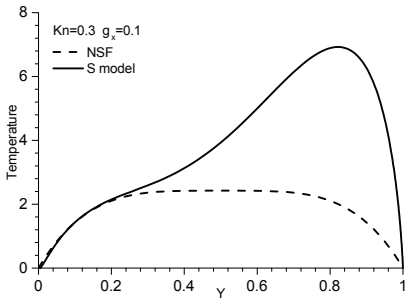

Figure 5: Force-driven Poiseuille flow; Comparison of cross-channel temperature profiles predicted by the S model and the NSF equation for $Kn = 0.3$ and $g_x = 0.1$. The temperature profiles as shown are the difference from a linear temperature distribution across the channel, fitted by using the gas temperatures at the upper and lower walls, amplified by a factor of 10000. For the NSF solutions, the velocity slip boundary condition is used at both walls, while the temperature jump boundary condition is used at the upper wall and the zero heat flux boundary condition is used at the lower wall.

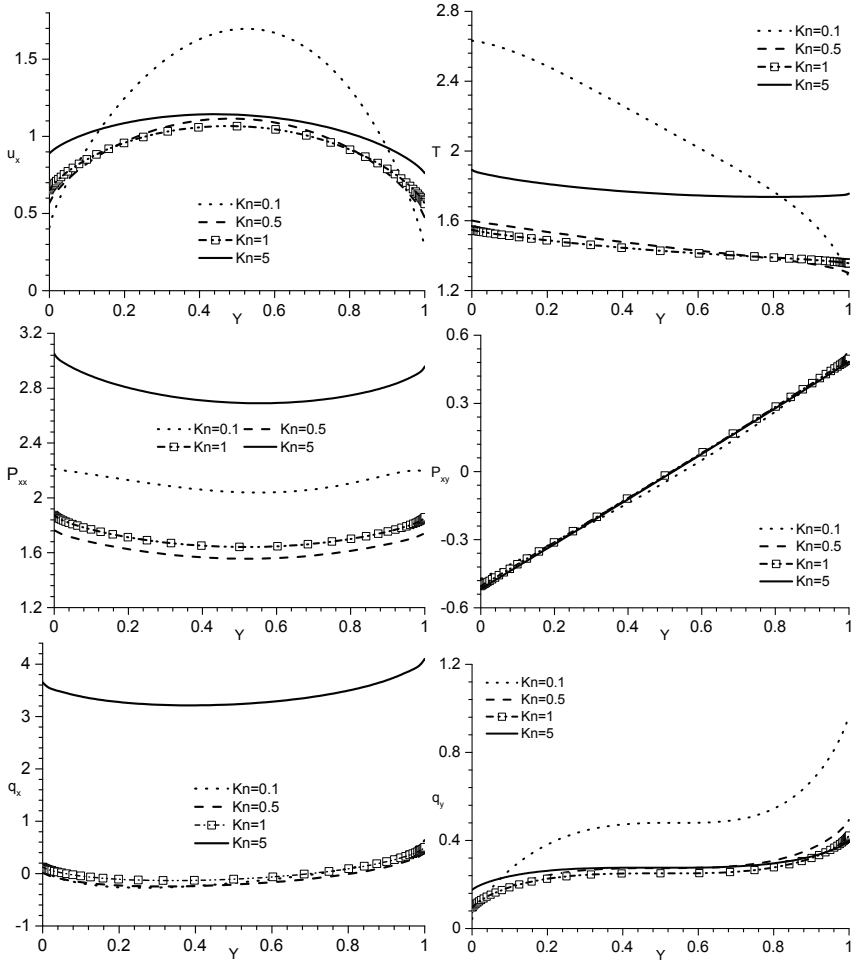

Figure 6: Profiles of macroscopic flow quantities in force-driven Poiseuille flows with $g_x = 1$. Zero-heat-flux boundary at $Y = 0$, fixed-temperature boundary at $Y = 1$.

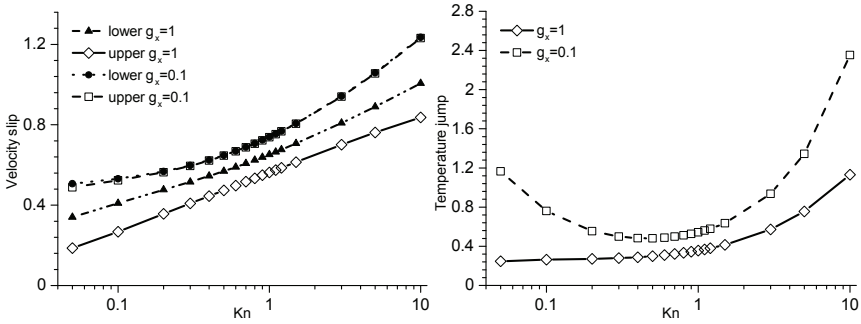

Figure 7: Force driven Poiseuille flow: velocity slip (left) at the lower (zero heat flux) and upper (fixed-temperature) plates, and temperature jump (right) at the upper plate. The velocity slip is re-normalized by the force magnitude, and the temperature jump is re-normalized by the square of the force magnitude.

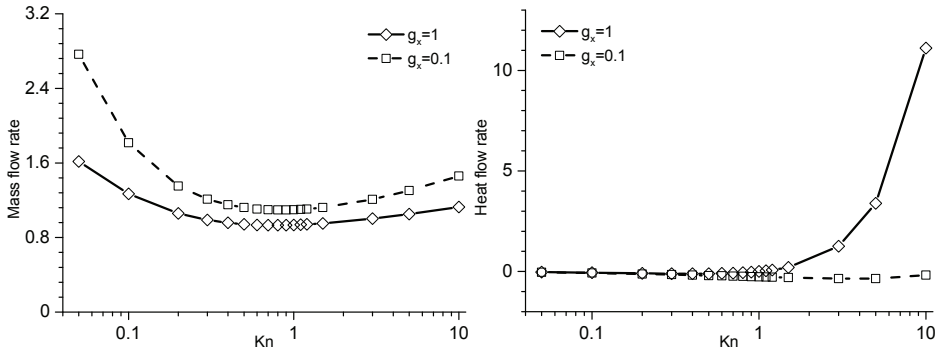

Figure 8: Mass and heat flow rates for force-driven Poiseuille flows of over a range of Kn. Both fluid quantities are re-normalized by the force magnitude.

5 Concluding remarks

We have investigated rarefied Couette and Poiseuille flows confined between two parallel plates, one with a specified heat flux (zero heat flux in this work) and the other with a fixed temperature. By numerically solving the S model, we have seen that the zero-heat-flux wall has a significant impact on the flowfield. Overall, the profiles of macroscopic fluid quantities can become unsymmetrical. Specifically, the temperature rises at the zero-heat-flux wall are higher than those at the fixed-temperature wall. When the viscous heating is strong (e.g. $U_w = 1.5$, and $g_x = 1$), the velocity slips at the two walls become significantly different from each other. An interesting span-wise heat flux jump phenomenon is observed at the zero heat flux wall. For the Poiseuille flows, the cross-channel temperature profiles are qualitatively different from hydrodynamic predictions, i.e. a bimodal-like distribution is found over a range of Knudsen numbers. Hence force-driven Poiseuille flow appears to be a good benchmark problem for testing the ability of extended hydrodynamic models to capture the zero-heat-flux wall effect.

Acknowledgments

This research was financially supported by the Engineering and Physical Sciences Research Council of the UK under Grant Nos. EP/I036117/1 and EP/I011927/1. Yonghao Zhang would like to thank the Royal Academy of Engineering and the Leverhulme Trust for the award of a RAEng/Leverhulme Senior Research Fellowship.

References

[1] M. S. Ivanov and S. F. Gimelshein. Computational hypersonic rarefied flows. Annu. Rev. Fluid Mech., 30(1) (1998), 469–505.

[2] C. M. Ho and Y .C. Tai. Micro-electro-mechanical-systems (MEMS) and fluid flows. Annu. Rev. Fluid Mech., 30(1) (1998), 579–612.
[3] G. A. Bird. Monte Carlo simulation of gas flows. Annu. Rev. Fluid Mech., 10(1) (1978), 11–31.
[4] S. M. Yen. Numerical solution of the nonlinear Boltzmann equation for nonequilibrium gas flow problems. Annu. Rev. Fluid Mech., 16(1) (1984), 67–97.
[5] G. A. Radtke, N. G. Hadjiconstantinou, and W. Wagner. Low-noise Monte Carlo simulation of the variable hard sphere gas. Phys. Fluids, 23(3) (2011), 030606.
[6] H. Struchtrup. Derivation of 13 moment equations for rarefied gas flow to second order accuracy for arbitrary interaction potentials. Multiscale Model.Simul., 3(1) (2005), 221–243.
[7] X. J. Gu and D. R. Emerson. A high-order moment approach for capturing non-equilibrium phenomena in the transition regime. J. Fluid Mech., 636(-1) (2009), 177–216.
[8] J. P. Meng, Y. H. Zhang, N. G. Hadjiconstantinou, G. A. Radtke, and X. W. Shan. Lattice ellipsoidal statistical BGK model for thermal non-equilibrium flows. J. Fluid Mech., 718 (2013), 347–370.
[9] H. Akhlaghi, E. Roohi and S. Stefanov, A new iterative wall heat flux specifying technique in DSMC for heating/cooling simulations of MEMS/NEMS, Int. J. Therm. Sci., 59 (2012), 111-125.
[10] Q. W. Wang, C. L. Zhao, M. Zheng and N. Y. E. Wu, Numerical investigation of rarefied diatomic gas flow and heat transfer in microchannel using dsmc with heat flux specified boundary conditiond part I: Numerical method and validation, Numerical Heat Transfer Part B, 53 (2008), 160-173.
[11] T. Klinc and I. Kušer Slip coefficients for general gas-surface interaction, Phys. Fluids, 15 (1972), 1018–1022
[12] A. A. Alexeenko, D. A. Levin, S. F. Gimelshein, R. J. Collins and G. N. Markelov. Numerical simulation of high-temperature Gas flows in a millimeter-Scale thruster , J. Therm. Heat Trans., 16 (2002), 10–16.
[13] G. N. Markelov, A. N. Kudryavtsev and M. S. Ivanov, Rarefaction effects on separation of hypersonic laminar flows, AIP Conference Proceedings, 585 (2001), 707.
[14] G. N. Markelov and M. S. Ivanov, Numerical study of 2D/3D micronozzle flows, AIP Conference Proceedings, 585 (2001), 539.
[15] N. Sengil and F. O. Edis. Implementation of parallel DSMC method to adiabatic piston problem. In Parallel Computational Fluid Dynamics 2007, volume 67 of Lecture Notes in Computational Science and Engineering, pages 75–82. Springer Berlin Heidelberg, 2009.
[16] A. Mohammadzadeh, E. Roohi, H. Niazmand, and S. Stefanov. Dsmc solution for the adiabatic and isothermal micro/nano lid-driven cavity. In Proceedings of the 3rd GASMEMS Workshop - Bertinoro, 2011.
[17] R. Kumar, E. Titov, and D. Levin. Comparison of statistical BGK and DSMC methods with theoretical solutions for two classical fluid flow problems. In Fluid Dynamics and Co-located Conferences, American Institute of Aeronautics and Astronautics, 2009.
[18] J. M. Burt and I. D. Boyd. Evaluation of a particle method for the ellipsoidal statistical Bhatnagar-Gross-Krook equation. In 44^{th} AIAA Aerospace Sciences Meeting and Exhibit, 2006.
[19] E. M. Shakhov. Generalization of the Krook kinetic relaxation equation. Fluid Dyn., 3(5) (1968), 95–96.
[20] E. M. Shakhov. Approximate kinetic equations in rarefied gas theory. Fluid Dyn, 3(1) (1968), 112–115.
[21] T. Platkowski and R. Illner. Discrete velocity models of the Boltzmann equation: A survey

on the mathematical aspects of the theory. SIAM Review, 30(2) (1988), 213–255.
[22] Y. Sone, Kinetic theory and fluid Dynamics, BIRKHÄUSER 2002.
[23] K. Aoki, S. Takata, and T. Nakanishi. Poiseuille-type flow of a rarefied gas between two parallel plates driven by a uniform external force. Phys. Rev. E, 65 (2002), 026315.
[24] J. P. Meng, L. Wu, J. M. Reese, and Y. H. Zhang. Assessment of the ellipsoidal–statistical Bhatnagar–Gross–Krook model for force-driven Poiseuille flows. J. Comput. Phys., 251(0)(2013), 383–395.